

Technical University of Denmark



Wave Optics Based LEO-LEO Radio Occultation Retrieval

von Benzon, Hans-Henrik; Høeg, Per

Published in:
Radio Science

Link to article, DOI:
[10.1002/2015RS005852](https://doi.org/10.1002/2015RS005852)

Publication date:
2016

Document Version
Peer reviewed version

[Link back to DTU Orbit](#)

Citation (APA):
von Benzon, H-H., & Høeg, P. (2016). Wave Optics Based LEO-LEO Radio Occultation Retrieval. *Radio Science*, 51(6), 589–602. DOI: 10.1002/2015RS005852

DTU Library

Technical Information Center of Denmark

General rights

Copyright and moral rights for the publications made accessible in the public portal are retained by the authors and/or other copyright owners and it is a condition of accessing publications that users recognise and abide by the legal requirements associated with these rights.

- Users may download and print one copy of any publication from the public portal for the purpose of private study or research.
- You may not further distribute the material or use it for any profit-making activity or commercial gain
- You may freely distribute the URL identifying the publication in the public portal

If you believe that this document breaches copyright please contact us providing details, and we will remove access to the work immediately and investigate your claim.

Wave Optics Based LEO-LEO Radio Occultation Retrieval

Hans-Henrik Benzon (hhvb@space.dtu.dk), Per Høeg (hoeg@space.dtu.dk)

The Technical University of Denmark, Space Division, Elektrovej Building 328, 2800
Kgs. Lyngby Denmark

1. Abstract

1 This paper describes the theory for performing retrieval of radio occultations that use
2 probing frequencies in the XK and KM band. Normally radio occultations use
3 frequencies in the L band and GPS satellites are used as the transmitting source and the
4 occultation signals are received by a GPS receiver on board a Low Earth Orbit (LEO)
5 satellite. The technique is based on the Doppler shift imposed, by the atmosphere, on the
6 signal emitted from the GPS satellite. Two LEO satellites are assumed in the occultations
7 discussed in this paper and the retrieval is also dependent on the decrease in the signal
8 amplitude caused by atmospheric absorption. The radio wave transmitter is placed on one
9 of these satellites while the receiver is placed on the other LEO satellite. One of the
10 drawbacks of normal GPS based radio occultations is that external information is needed
11 to calculate some of the atmospheric products such as the correct water vapor content in
12 the atmosphere. These limitations can be overcome when a proper selected range of high
13 frequency waves are used to probe the atmosphere. Probing frequencies close to the
14 absorption line of water vapor have been included, thus allowing the retrieval of the water
15 vapor content. Selecting the correct probing frequencies would make it possible to
16 retrieve other information such as the content of ozone. The retrieval is performed
17 through a number of processing steps which are based on the Full Spectrum Inversion
18 (FSI) technique. The retrieval chain is therefore a wave optics based retrieval chain and it
19 is therefore possible to process measurements that include multipath. In this paper
20 simulated LEO to LEO radio occultations based on 5 different frequencies are used. The
21 5 frequencies are placed in the XK or KM frequency band. This new wave optics based

22 retrieval chain is used on a number of examples and the retrieved atmospheric parameters
23 are compared to the parameters from a global ECMWF analysis model. This model is
24 used in a forward propagator that simulates the electromagnetic field amplitudes and
25 phases at the receiver on board the LEO satellite.

26

27 LEO-LEO cross-links radio occultations using high frequencies are a relative new
28 technique and the possibilities and advantages of the technique still needs to be
29 investigated. The retrieval of this type of radio occultations is considerable more
30 complicated than standard GPS to LEO radio occultations, because the attenuation of the
31 probing radio waves is used in the retrieval and the atmospheric parameters are found
32 using a least square solver. The best algorithms and the number of probing frequencies
33 that is economical viable must also be determined. This paper intends to answer some of
34 these questions using end to end simulations.

35 **2. Introduction**

36 It is well known from the literature that GPS-LEO radio occultation sounding can lead to
37 derivation of atmospheric parameters like temperature, pressure and humidity, based on
38 the bending of the emitted signal due to variations in the refractive index, see [*Benzon et*
39 *al.*, 2015]. These data are increasingly considered for numerical weather prediction and
40 climate models. Space missions such as GPS/MET, CHAMP and METOP clearly
41 indicate that temperature in large part of the atmosphere can be estimated with an
42 accuracy of 1 K. However, when it comes to determination of humidity in the atmosphere
43 based on GPS-LEO measurements, there is a need for a priori estimates of the
44 temperature. Water vapor is a major greenhouse gas and due to its large abundance, it
45 significant influences the climate. Also, due to the large energy transfers associated with
46 the phase transitions of water it impacts the short term dynamics of the atmosphere
47 considerably e.g. by stimulating the development of tropical hurricanes. Therefore, an
48 accurate knowledge of the temporal and spatial water vapor distribution is desirable. In
49 order to avoid use of external data more sophisticated satellite systems have been
50 proposed where the atmosphere is sounded through LEO-LEO cross-links [*Høeg and*
51 *Kirchengast*, 2002, *Kursinski et al.*, 2002; *Eriksson et al.*, 2003]. The carrier frequencies
52 used in these LEO-LEO links must be located around a water vapor absorption line to
53 enable detection of both phase and amplitude modulations caused by the atmosphere.

54

55 It is essential, for each probing frequency, to correctly retrieve the complex refraction
56 index [*Schweitzer et al.* 2011]. This paper also contains end to end simulations for LEO-

57 LEO links using 3 or 5 probing radio waves with frequencies near absorption lines. The
58 retrievals are based on bending angle and transmission profiles calculated from geometric
59 optics while the atmospheric state variables are calculated using the iterative Best Linear
60 Unbiased Estimation (BLUE) algorithm. A discussion of important GPS radio occultation
61 and LEO-LEO cross link missions and proposals can also be found in the paper. Under
62 the assumption of spherical symmetry, a complex refractivity profile is readily computed,
63 through Abel transforms, from a profile of bending angle and a profile of transmission
64 (optical depth) measured as functions of ray impact parameter [*Kursinski et al.* 2002].
65 Wave optics based retrieval techniques such as Full Spectrum Inversion (FSI), Canonical
66 Transform CT or geometric optics can be used to calculate the bending angle and
67 transmission height profiles. [*Kursinski*, 2002] describes how transmission profiles can be
68 computed using geometrical optics whereas [*Gorbunov*, 2002] suggests the use of the
69 canonical amplitude in order to establish the transmission profile. The major advantage of
70 wave optics based methods as compared to geometrical optics is that the former methods
71 can disentangle multipath [*Gorbunov*, 2002, *Jensen et al.* 2003 and *Jensen et al.* 2004].
72 This disentanglement of multipath gives a lower noise level in the retrieved parameters in
73 case of multipath. A wave optics based retrieval chain based on FSI will be used in this
74 study.

75

76 Alternatively, atmospheric parameters can also be derived from observations of the
77 variations in the absorption coefficient with frequency by using pairs of frequencies
78 (calibrations frequencies/tones) [*Kursinski et al.* 2002, *Nielsen et al.* 2003, *Gorbunov et.*
79 *al.* 2007]. In this approach atmospheric parameters are derived from a profile of real

80 refractivity plus measured variations in imaginary refractivity as function of frequency.
81 These variations are computed by an Abel transform, assuming spherical symmetry, of a
82 profile representing the differences between two absorption profiles computed at two
83 different frequencies.

84

85 Improved RO satellite missions with potential of determination of both temperature and
86 humidity without a priori information has been proposed, see [*Høeg and Kirchengast,*
87 2002] and the needed retrieval techniques have been presented [*Kursinski et al., 2002* and
88 *Gorbunov et. al., 2005*]. In the simulation study presented here, we simulate the concept
89 of using 5 different frequencies in the XK and KM frequency band respectively. The
90 radio occultation's are performed by two LEO satellites one of them transmitting radio
91 signals at 5 different frequencies. By measuring not only the phase but also the amplitude
92 variations of the signals unambiguous retrieval of temperature, pressure and humidity
93 profiles is made possible. Key components of this new LEO-LEO retrieval chain is the
94 FSI and the trust-region solver that calculates the atmospheric parameters from the
95 complex refractivity's. A statistical analysis performed on the simulations reveals the
96 level of accuracy and precision that can be expected from the technique.

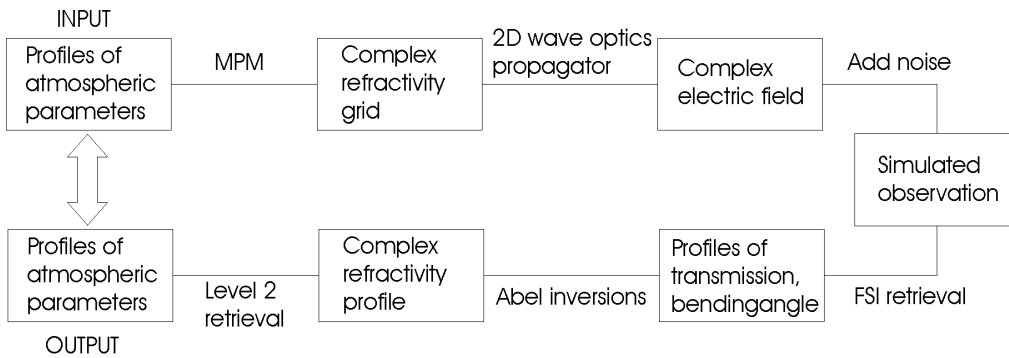
97

98

99 **3. Retrieval of LEO-LEO radio occultations**

100 This section presents a discussion of the wave optics based LEO-LEO retrieval chain.
 101 The atmospheric propagation of the LEO-LEO signals and the data analysis is studied
 102 using a sequence of simulation elements. Each element processes the output of the
 103 previous element and generates the input of the following element. In all simulations the
 104 refractivity field is assumed to be spherically symmetric, i.e., $N(\vec{r})=N(r)$. The total end
 105 to end simulation chain is depicted in Figure 1.

106
 107



108

109 **Figure 1.** Overview of the simulation processing chain.

110

111 First, atmospheric parameter inputs (temperature, pressure and humidity) are transformed
 112 to a complex refractivity field using a Millimetre-wave Propagation Model (MPM).
 113 Subsequently, this field is applied in the wave optics propagation simulations that yield
 114 the electromagnetic field along the receiver orbit. These fields are used as the starting
 115 point for the retrieval. The retrieval starts by calculating the bending angle and
 116 transmission profiles for each of the probing frequencies using the Full Spectrum

117 Inversion (FSI) technique. These profiles are then inverted into complex refractivity
118 profiles through Abel inversions. Finally, the profiles of atmospheric parameters are
119 retrieved through a non-linear least square fit. In the following, these different processing
120 steps are described.

121

122 **Retrieval of bending angle and transmission based on FSI**

123 Our retrieval scheme is based on the Full Spectrum Inversion (FSI) method [*Jensen et al.*
124 2003]. The FSI technique applies a Fourier transform and uses the derivative of the phase
125 after this transformation. Time and instantaneous frequency are the output from FSI –
126 also in case of multipath, where there will be more Doppler frequencies at a given time.
127 The Fourier amplitudes describe the distribution of energy with respect to impact
128 parameter only modulated by signal spreading and absorption, i.e., defocusing is
129 automatically accounted for.

130

131 When using Full Spectrum Inversion to invert radio occultation data, a distinction
132 between ideal occultations and realistic occultations must be made. Ideal occultations are
133 defined as occultations with a spherical Earth and perfect circular orbits lying in the same
134 plane. On the other hand, realistic occultations are defined as occultations with an oblate
135 Earth and approximately circular orbits lying in two different planes. In the former case, a
136 global Fourier transform can be applied directly to the measured signal; and pairs of ray
137 arrival time, t_0 , and ray Doppler angular frequency, ω_0 , is related through:

138

139
$$(\omega(t_0), t_0) = \left(\omega_0, - \left| \frac{d \arg(F)}{d\omega} \right|_{\omega=\omega_0} \right) \quad (1)$$

140

141 where F represents the Fourier transform of the measured signal. Realistic occultations
 142 require that the occultation signal and ephemeris data are re-sampled with respect to the
 143 opening angle, θ , between the radius vectors of the satellites and that frequency
 144 variations caused by radial variations in the radius vectors are removed before the
 145 equation above is applied, see [Jensen et al. 2003]. When the variations in the Doppler
 146 frequency have been determined through equation (1), then the bending angle profile can
 147 be found from the standard equations, see e.g. [Kursinski et al. 2000].

148

149 The corresponding transmission profile is determined by expressing the Fourier
 150 amplitudes with respect to impact parameter and by correcting the amplitudes for
 151 spreading modulations. The transmission, i.e. the normalized intensity, is related to the
 152 ray amplitude data through

153

154
$$\xi(a) = \frac{I(a)}{I_m(a)} = \frac{A^2(a)}{A_m^2(a)} \quad (2)$$

155

156 where I is the intensity of the signal in the absence of spreading and defocusing, I_m is the
 157 intensity the signal would have had without absorption, spreading and defocusing, and A
 158 and A_m are the corresponding amplitudes. The Fourier amplitude is related to the
 159 occultation geometry through

160

$$161 \quad |F(a)|^2 = \xi(a) \frac{P}{2\pi} \cdot \frac{a}{r_G r_L \sin(\theta) \sqrt{r_G^2 - a^2} \sqrt{r_L^2 - a^2} \left(\frac{d\theta}{da}\right)^2 k} \quad (3)$$

162

163 [Jensen *et al.* 2003]. Here P is the transmitter power, r_G and r_L are the distances from the
 164 center of curvature to the transmitter and receiver, respectively, and θ is the angle
 165 between these. This expression is valid in general for a 3-D geometry with circular orbits.
 166 For non-circular orbits, additional terms are introduced in (3) as demonstrated in
 167 [Gorbunov and Lauritsen, 2004]. Since the simulated electromagnetic field is two-
 168 dimensional, spreading corrections are only performed for spreading within the
 169 occultation plane. Without transverse effects a factor of $a/(r_G r_L \sin(\theta))$ disappear from
 170 (3). In this case the Fourier amplitude becomes

171

$$172 \quad |F(a)|^2 = \xi(a) \frac{P}{2\pi} \cdot \frac{1}{\sqrt{r_G^2 - a^2} \sqrt{r_L^2 - a^2} \left(\frac{d\theta}{da}\right)^2 k} \quad (4)$$

173

174 where the transmitter power P is assumed constant throughout the occultation. From the
 175 discussion, it follows that a profile of transmission multiplied by the transmitted power is
 176 readily computed through (2) and (4). The transmitted power in the direction of the
 177 receiving satellite may not be known with a high accuracy, however, as long as the
 178 transmitted power is constant this will not affect the inversion; this will be shown in the
 179 following section.

180

181 The FSI method has a number of advantages related to Leo-Leo occultations:

182

- 183 • it disentangles multipath
- 184 • defocusing is automatically accounted for
- 185 • it is simple, both conceptually and computationally

186

187 The major drawback of the FSI technique is that it relies on the assumption of local
188 spherical symmetry. When this assumption is not fulfilled, the method may not be able to
189 disentangle multipath. Like other methods based on Fourier Integral Operators, the FSI
190 amplitude always suffers from minor amplitude oscillations caused by Gibb's
191 phenomenon which may cause unwanted artificial oscillations in the retrieved
192 transmission profiles [*Lohmann et al.* 2006 and *Gorbunov et al.* 2004]. The problem of
193 Gibb's phenomenon can be solved by using appropriate window functions in the
194 evaluation of the Fourier transform as described in [*Lohmann et al.* 2006].

195

196 **Retrieval of complex refractivity**

197 Given profiles of bending angle and transmission as function of impact parameter the
198 complex refractivity is derived. The real part of the refractivity is derived from the
199 bending angle profile using the standard Abel inversion as described in e.g. [*Fjeldbo,*
200 1971]. Here focus will be on retrieval of the imaginary part of the refractivity, which is
201 directly related to the absorption. The imaginary refractivity is given by

202

203

$$N'' = 10^6 \cdot n'' = 10^6 \cdot (2k)^{-1} \cdot \alpha \quad (5)$$

204

205 where k is the free space wave number, n'' is the imaginary part of the refractive index

206 and α is the absorption coefficient per unit distance in the medium [Born and Wolf, 1999].

207 The absorption coefficient is calculated using an inverse Abel integral of the signal

208 transmission [Kursinski et al., 2002],

209

210

$$\alpha(a) = \frac{1}{\pi} \frac{da}{dr} \Big|_{a'=a} \int_a^\infty \frac{d \ln \xi}{da} \frac{da'}{\sqrt{a'^2 - a^2}} \quad (6)$$

211

212 where r is the ray path perigee distance to the curvature center, a is the impact parameter

213 and ξ is the transmission defined above. From the equation it follows that the

214 transmission enters the Abel integral as the derivative of the logarithm of the transmission.

215 The transmission may, therefore be scaled with any arbitrary constant without affecting

216 the results of the Abel integral. This explains why it is not a problem for the inversion

217 that the transmission derived from FSI is scaled by the unknown transmitted power. The

218 reason for this is that the signal absorption is related to the relative variations in the signal

219 intensity and not the absolute variations. Consequently, there will be no need for

220 calibration of the measured amplitudes, as the observations will not be affected by long-

221 term drifts in the instrument, which makes the technique very suitable for climate

222 monitoring.

223

224 **Retrieval of atmospheric parameters**

225 Given the retrieved profiles of both real and imaginary refractivity for the 5 frequencies,
226 and assuming hydrostatic balance, a solution for dry pressure, temperature and water
227 vapor pressure can be found. The 5 real refractivity profiles only constitute one piece of
228 independent information as the atmosphere is virtually non-dispersive for the frequency
229 ranges under consideration. Consequently, the system contains 7 pieces of independent
230 information and three unknowns. A least square (LS) fitting method is employed for this
231 over-determined problem. It is worth to notice that if the signals had also been subject to
232 absorption caused by liquid water, e.g. rain, then the system would have contained an
233 additional unknown parameter, liquid water. However, there will also in this case be a
234 slight redundancy in the number of equations.

235

236 In order to exploit the information given by the hydrostatic equation in a simple manner,
237 the inversion is started at the topmost layer corresponding to the largest altitudes where
238 reliable observations can be achieved. Boundary conditions for the “*unknown*”
239 *parameters* p , T and e are specified at this level. In the current simulations the “true”
240 atmospheric parameters are used as the upper boundary conditions. These parameters are
241 then used to calculate an initial guess for the solution at the next level below. The initial
242 guess is adjusted through minimization of a set of appropriate functions by the LS
243 algorithm. The functions to be minimized reflect the information contained in the derived
244 refractivity’s and the hydrostatic balance assumption. The function representing the
245 hydrostatic balance constraint is implemented using

246

247
$$p_i = p_{i-1} + \Delta p \approx p_{i-1} + g \cdot \tilde{\rho}_i \cdot \Delta h_i = p_{i-1} + \frac{g}{2} \left(\frac{p_i}{RT_i} + \frac{p_{i-1}}{RT_{i-1}} \right) (h_i - h_{i-1}) \quad (7)$$

248

249 where ideal gas behavior and linear density, ρ , variations between the levels have been
 250 assumed. The level index, i , is counted downwards from the topmost level and g is the
 251 gravitational acceleration, R is the gas constant, h is geometric height and p is pressure.
 252 Equation (7) expresses the bound on the solution at the i 'th level imposed by the solution
 253 from the level above. By rearranging this expression and including the information from
 254 the retrieved refractivity's an error function $J(p_i, T_i, e_i)$ can be constructed. This function
 255 must be minimized at each level with respect to the unknowns p_i , T_i and e_i :

256

$$\begin{aligned}
 J(p_i, T_i, e_i) = & \left[\left(p_{i-1} + \frac{gp_{i-1}}{2RT_{i-1}} (h_i - h_{i-1}) \right) - \left(p_i - \frac{gp_i}{2RT_i} (h_i - h_{i-1}) \right) \right]^2 \\
 & + (N'_i - N'(p_i, T_i, e_i))^2 \\
 & + (N''_{i,1} - N''(p_i, T_i, e_i, f_1))^2 \\
 257 & + (N''_{i,2} - N''(p_i, T_i, e_i, f_2))^2 \quad (8) \\
 & + (N''_{i,3} - N''(p_i, T_i, e_i, f_3))^2 \\
 & + (N''_{i,4} - N''(p_i, T_i, e_i, f_4))^2 \\
 & + (N''_{i,5} - N''(p_i, T_i, e_i, f_5))^2
 \end{aligned}$$

258

259 The first line in the error function above represents the squared error in the hydrostatic
 260 balance equation. The remaining terms represents the squared differences between the
 261 retrieved refractivity's and the corresponding refractivity's derived from the Liebe MPM

262 model for p_i , T_i and e_i . In the Liebe model the magnetic field, droplet density and rain rate
263 contributions are neglected.

264

265 The error function given by (8) is non-linear and is minimized using a non linear trust-
266 region solver. The Trust-Region (TR) algorithms are relatively new iterative methods for
267 solving nonlinear optimization problems. They are widely used in power engineering,
268 finance, applied mathematics, mechanical engineering, and other areas. The TR methods
269 have global convergence and local super convergence, which differentiates them from
270 line search methods and Newton methods. The TR methods have better convergence
271 when compared with widely-used Newton-like methods. The main idea behind a TR
272 algorithm is calculating a trial step and checking if the next values of x belong to the *trust*
273 *region*, see [Sorensen 1982]. Calculation of the trial step is strongly associated with the
274 approximation model, which here is the Liebe model. In the solution procedure the
275 retrieved atmospheric parameters at one level is used as the initial guess at the next level.

276

277 During the occultations the signals can get so attenuated that the imaginary refractivity's
278 get so small that the corresponding equations in (8) can not be used. Information from the
279 real refractivity is only lost in the extreme situation where neither of the signals can be
280 measured. The portions of the atmosphere where information from the imaginary
281 refractivity's could be lost are related to very wet or dry regions. In the lower troposphere,
282 it is expected that the 23 GHz (and higher) signal may be completely attenuated due to
283 high concentrations of water vapor - this will especially be the situation in the tropics. In
284 the upper troposphere, the concentration of water vapor is expected to be so low that the

285 absorption of the signal may not contain any useful information. This may also be the
286 case for the other frequencies in the system when the atmosphere is very dry (for instance
287 in the stratosphere), in these cases it will not be possible to retrieve the concentration of
288 water vapor.

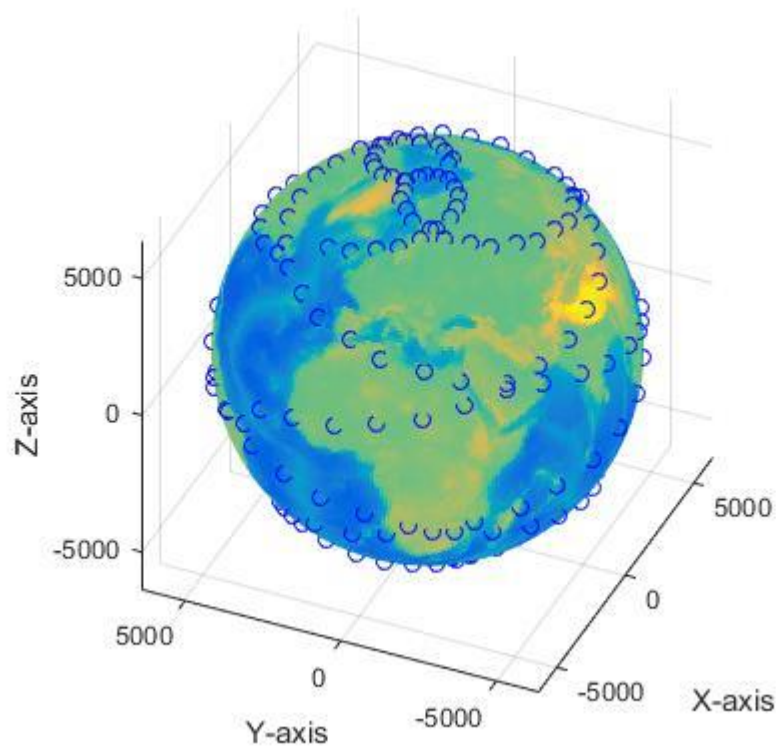
289 **4. XK and KM frequency range radio occultations**

290 A large number of simulations both in the XK and in the KM frequency band have been
291 performed in order to validate the retrieval scheme. The frequencies in the XK range
292 contain three frequencies around the 22 GHz water vapor absorption line and two lower
293 frequencies while the frequencies in the KM range contain the same three frequencies
294 around the 22 GHz water vapor line plus two additional frequencies near the 183 GHz
295 absorption line. These frequencies are selected in accordance with international radio
296 frequency regulations, which forbid use of frequencies directly around line center for
297 active sounding.

298

299 The forward simulations have been performed using the End-to-End Generic Occultation
300 Performance Simulation and Processing System version 5 (EGOPS5) software
301 [*Kirchengast et al. 2007, Fritzer et al. 2010*]. Two transmitting LEO satellites at a height
302 of 800 km and two counter rotating receiver LEO satellites at a height of 600 km was
303 used to simulate the radio occultations. All of the satellites are assumed to follow a sun
304 synchronous orbit. The atmosphere model used in the simulations was extracted from a
305 global ECMWF analysis for a specific northern hemisphere summer day. In order to
306 simulate the effect of atmospheric turbulence noise is added to the forward modeled
307 excess phase and amplitude. This noise is generated following the principles found in
308 [*Gorbunov and Kirchengast, 2007*]. Noise simulating the observation system errors was
309 also superimposed on the simulated radio occultations. The simulated error sources
310 include thermal noise, drift errors and precise orbit errors. Ionospheric scintillations are

311 not included in the simulations because the corresponding noise level will be very low
312 due to the high probing frequencies. The atmospheric model used in the forward
313 simulations will for simplicity in the following be called the GRAZ atmosphere model.
314 More details on the forward simulations can be found in [Schweitzer *et al.* 2011].
315



316 **Figure 2.** Positions of simulated LEO-LEO radio occultations.
317
318

319 The simulations can be classified in the 4 different classes listed below. The positions of
320 the radio occultations can be seen in Figure 2.

321

322 1) The forward simulation of the electromagnetic field has been performed in clear air
323 and the electromagnetic field frequencies are in the XK frequency range.

324

325 2) The forward simulation of the electromagnetic field has been performed in a cloudy
326 atmosphere that generates atmospheric scintillations. The electromagnetic field
327 frequencies are in the XK frequency range.

328

329 3) The forward simulation of the electromagnetic field has been performed in clear air
330 and the electromagnetic field frequencies are in the KM frequency range.

331

332 4) The forward simulation of the electromagnetic field has been performed in a cloudy
333 atmosphere that generates atmospheric scintillations. The electromagnetic field
334 frequencies are in the KM frequency range.

335

336 101 simulation runs have been performed for each of these classes and a statistical
337 analysis has been performed based on these simulations. The earth is divided into 3 parts
338 corresponding to 3 different latitude intervals. These intervals are tropics 20°S to 20°N,
339 northern hemisphere 30°N to 90°N, and southern hemisphere 90°S to 30°S. The 101
340 simulation runs for each of the 4 classes is selected in such a way that the 3 latitude
341 intervals are represented equally in the simulations. The table below summarizes the
342 simulations

343

	<i>Probing radio wave</i>	<i>Meteorological</i>	<i>Number of cases</i>
	<i>Frequencies</i>	<i>conditions</i>	

Simulation Class 1	9 GHZ 13.5 GHZ 17.25 GHz 20.2 GHZ 22.6 GHz	Clear air	101
Simulation Class 2	9 GHZ 13.5 GHZ 17.25 GHz 20.2 GHZ 22.6 GHz	Turbulent and cloudy air	101
Simulation Class 3	17.25 GHz 20.2 GHz 22.6 GHz 179.0 GHz 181.95 GHz	Clear air	101
Simulation Class 4	17.25 GHz 20.2 GHz 22.6 GHz 179.0 GHz 181.95 GHz	Turbulent and cloudy air	101

344 **Table 1.** Simulation classes and the corresponding conditions.

345 The statistical analysis performed for each of the 4 classes calculates 4 different statistical
346 parameters. These parameters are absolute bias (BIAS), normalized bias (NBIAS),
347 standard error of the difference (SED) and normalized standard error of the difference
348 (NSED). The absolute bias is defined as the mean value of the absolute error and it can be
349 estimated by the follow equation

350

351

$$BIAS = \frac{1}{N} \sum_{i=1}^N (x_{mi} - x_{vi}) \quad (9)$$

352

353 where N is the number samples and x_{vi} and x_{mi} is the i 'te sample of the true and measured
354 value respectively.

355

356 The normalized bias (NBIAS) is defined as the mean value of the absolute error
357 normalized with respect to the mean true value. This parameter can be estimated with the
358 following equation

359

360

$$NBIAS = \frac{\frac{1}{N} \sum_{i=1}^N (x_{mi} - x_{vi})}{\frac{1}{N} \sum_{i=1}^N x_{vi}} \quad (10)$$

361

362 The standard error of the difference (SED) is defined as the standard deviation of the
363 absolute error and is estimated by the following equation

364

365

$$SED = \sqrt{\frac{1}{N} \sum_{i=1}^N (x_{mi} - x_{vi} - BIAS)^2} \quad (11)$$

366

367 The normalized standard error of the difference (NSED) is defined as the standard
368 deviation of the absolute error normalized with respect to the mean value of the true value
369 and is estimated by the following equation

370

371

$$NSED = \frac{\sqrt{\frac{1}{N} \sum_{i=1}^N (x_{mi} - x_{vi} - BIAS)^2}}{\frac{1}{N} \sum_{i=1}^N x_{vi}} \quad (12)$$

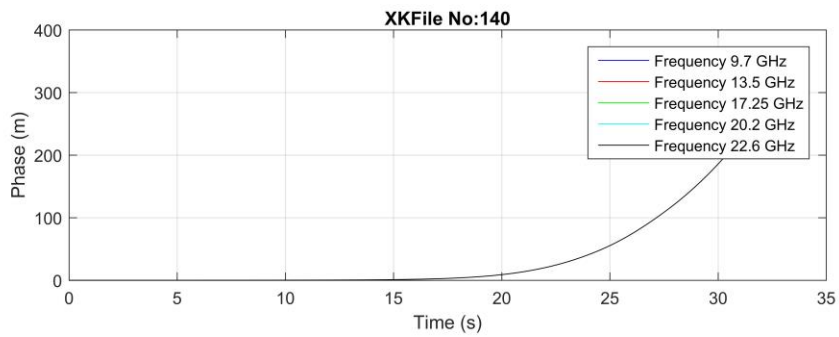
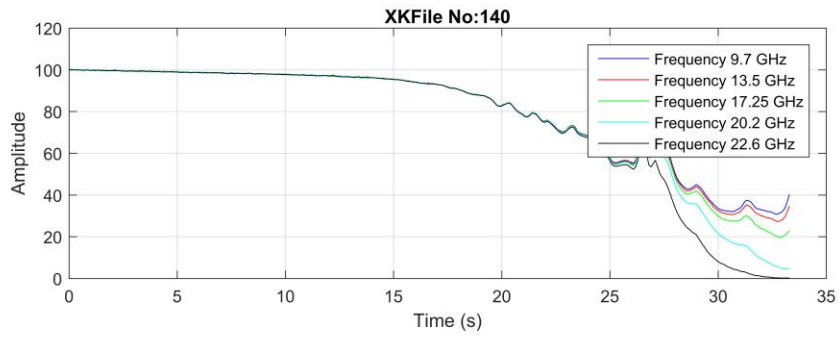
372

373 The following three subsections contain some of the simulation results performed during
 374 the study. The simulation results in the first subsection correspond to simulation class 1
 375 while the simulations in the second subsection correspond to simulations in simulation
 376 class 4.

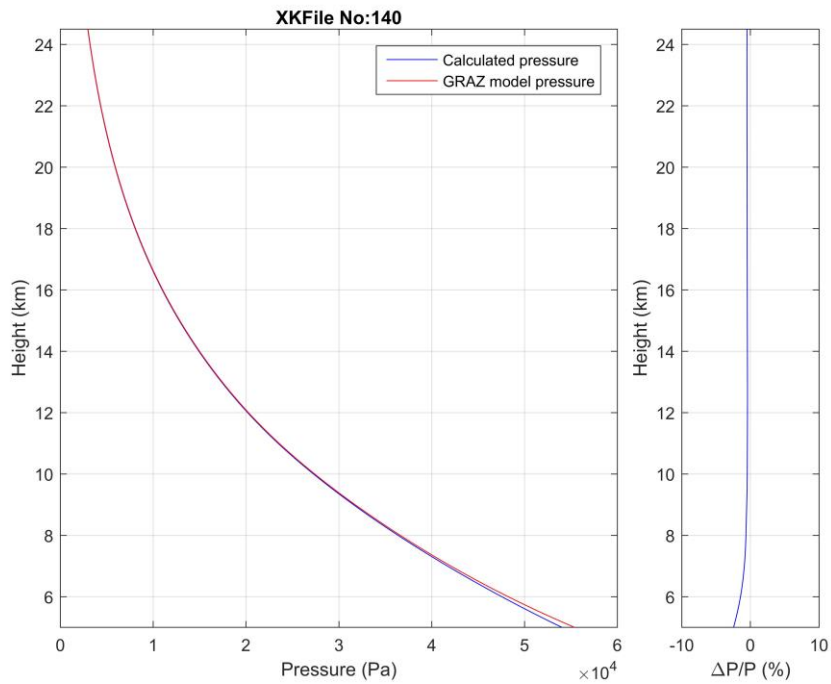
377 **4.1 Comparing XK based retrievals in clear air with corresponding values in the**
 378 **GRAZ model**

379 The forward simulation of the LEO-LEO radio occultation signals has here been
 380 performed in clear air. The GRAZ atmosphere model has been used to calculate the
 381 complex refractivity field in the forward propagator that simulates the radio occultation
 382 measurements. The corresponding pressure, temperature and specific humidity height
 383 profiles can also be extracted from the model. These atmospheric height profiles are
 384 compared to the retrieved parameters. Results from one of the 101 simulations are
 385 presented in Figure 3.

386

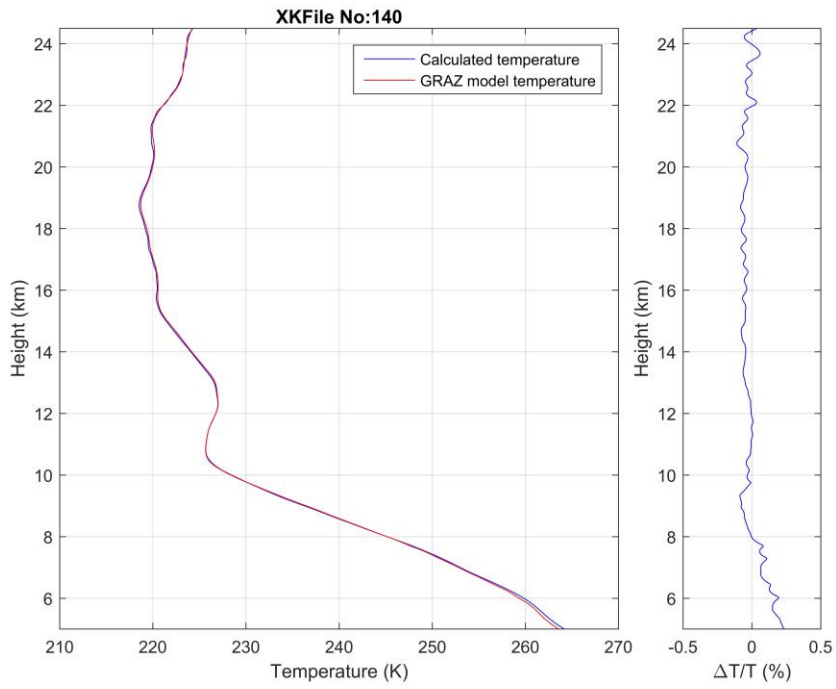


387 (A)

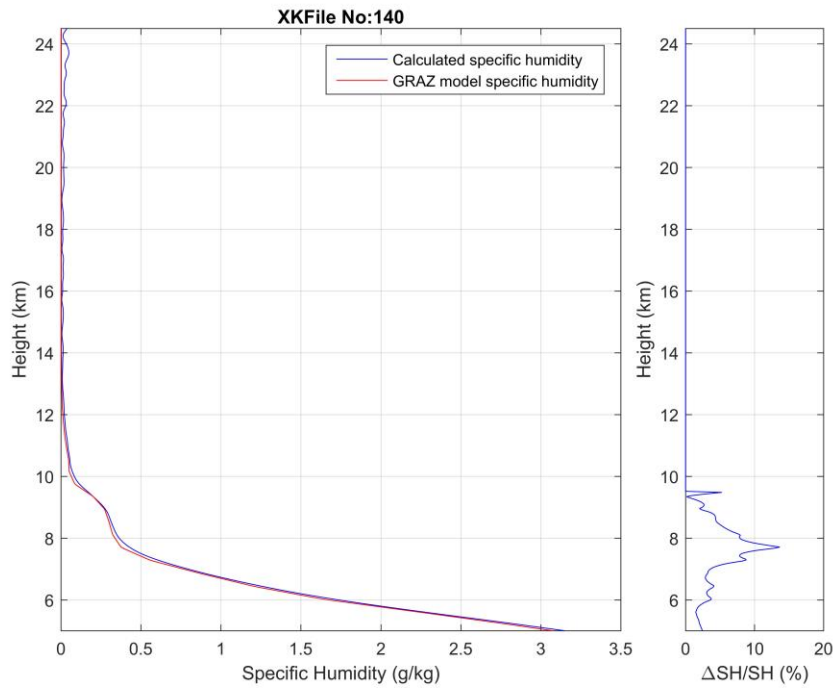


388

389 (B)



390 (C)



391

392 (D)

393 **Figure 3.** (A) The amplitude and phases for the 5 different frequencies. The mean
394 latitude and longitude for the tangent point is 77.86 degrees and 104.02 degrees
395 respectively for this rising occultation. The condition for the simulation is clear air and
396 probing frequencies in the XK range. (B) The pressure versus height. The blue curve is
397 the retrieved pressure while the red curve is the GRAZ model. (C) The temperature
398 versus height. The blue curve is the retrieved temperature while the red curve is the
399 GRAZ model. (D) The specific humidity versus height. The blue curve is the retrieved
400 specific humidity while the red curve is the GRAZ model. Panels (B) to (D) all have a
401 blue curve on the right side which is the relative difference between the retrieved values
402 and the GRAZ model values.

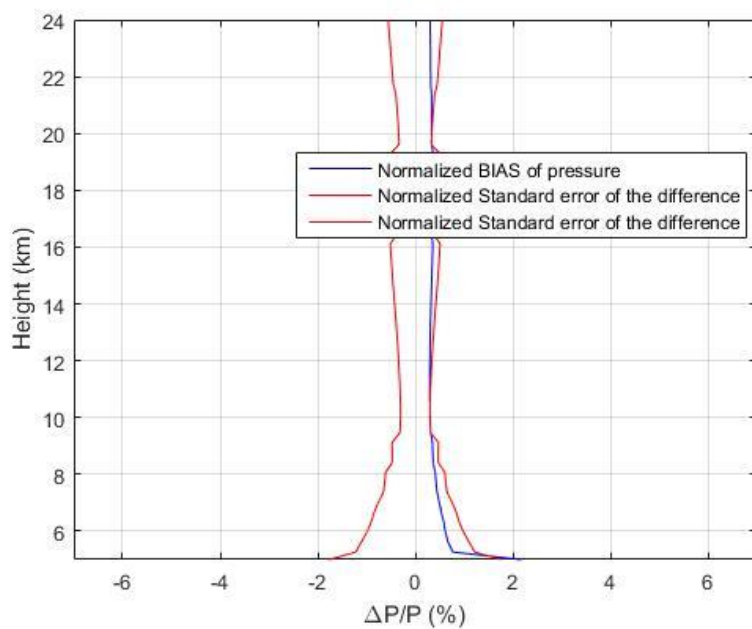
403

404 Figure 3 (A) shows the radio occultation amplitudes and phases as a function of time for
405 the 5 probing XK frequencies. These curves are the starting point for the retrieval process.
406 The results of the solver are presented in Figure 2 (B)-(D). These plots show the
407 calculated (blue curve) pressure, temperature and specific humidity profiles together with
408 the corresponding (red curve) model profiles. The relative difference between the
409 retrieved physical parameters and the model values are represented with the blue curves
410 on the right side of the plots. It's seen from the plots that there is a good agreement
411 between retrieved atmospheric parameters and the corresponding model parameters. The
412 specific humidity is in general determined with the lowest precision, but it is still relative
413 precise as long as all of the frequencies are present. The height at which the radio wave is
414 absorbed in the atmosphere decrease with decreasing frequency, so the number of
415 independent equations decrease for heights approaching the earth surface leading to lower

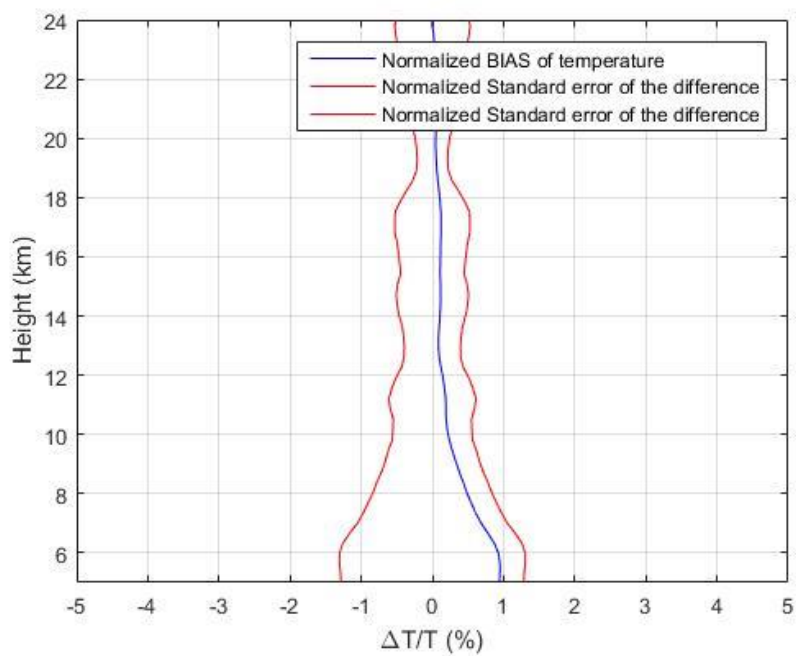
416 precision in the retrieved parameters. The lowest height in the plots is approximately 5

417 km, ensuring that all of the probing frequencies are used in the retrieval.

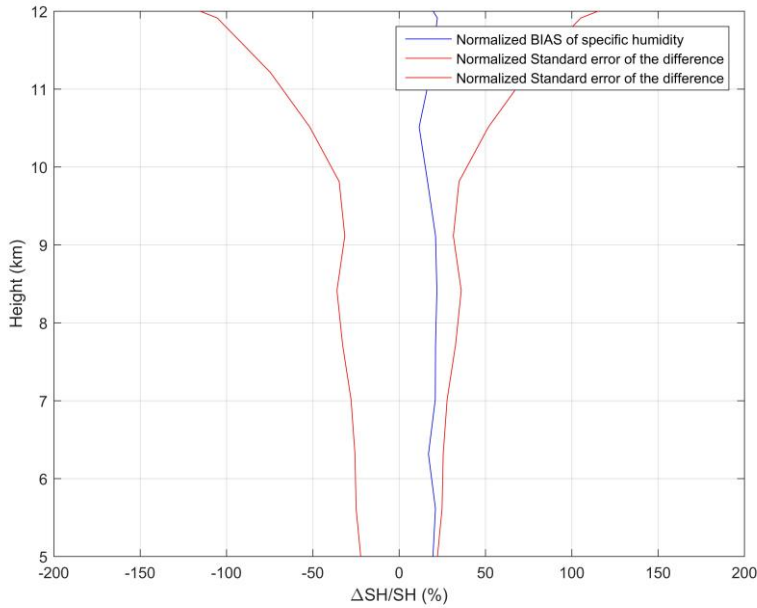
418



419 (A)



420 (B)



421

422 (C)

423 **Figure 4.** (A) The normalized pressure bias (blue curve) and normalized standard error of
 424 the difference for pressure (red curve) in (%) as a function of height. (B) The normalized
 425 temperature bias (blue curve) and normalized standard error of the difference for
 426 temperature (red curve) as a function of height. (C) The normalized specific humidity
 427 bias (blue curve) and normalized standard error of the difference for specific humidity
 428 (red curve) in (%) as a function of height.

429

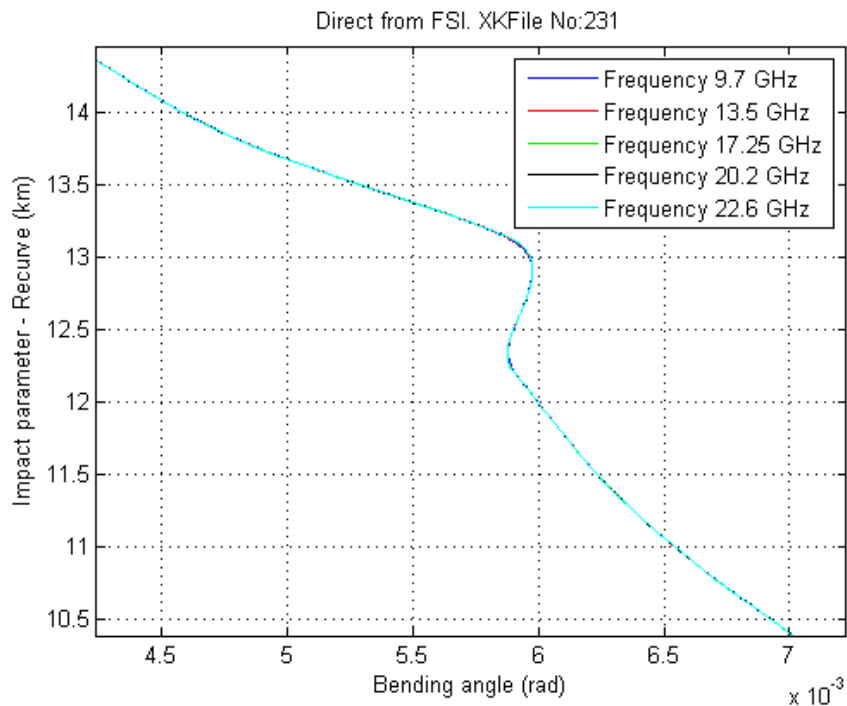
430 Figure 4 shows the result of the statistical analysis. All of the 101 simulations are used in
 431 the statistical plots. The statistical analysis is performed for 3 atmospheric parameters,
 432 pressure, temperature and specific humidity. The blue curves represent the bias and the
 433 red curves represent the standard error of the difference between retrieved and model
 434 values. It is seen that the bias and standard error of the difference all fall within an

435 acceptable error level. It is also seen that the bias and standard error of the difference for
436 pressure and temperature are very small at high altitudes but increase for decreasing
437 altitudes. There are not any measurements at low altitudes and the complex refractivity
438 values are therefore found from an extrapolation of the curves. The extrapolated values
439 are found from a polynomial fit to the curves. This will in many cases lead to an error in
440 the retrieved parameters at low altitudes and hence an increase in the bias level.

441

442 Some of the simulations contain multipath. Figure 5 shows such a case. The bending
443 angle profile for one of the XK simulations in clear air is here shown as a function of ray
444 height which is the difference between impact parameter and the local earth curvature. It
445 is seen that all of the probing waves have as expected the same bending angle profile.

446



447

448

449 **Figure 5.** Closer look at the bending angle versus impact parameter for the 5 frequencies
450 calculated using FSI. The bending angle profiles show the characteristic S-signature
451 which is a sign of multipath.

452

453 The bending angle profiles show the characteristic S-signature which is a sign of
454 multipath. Using a wave optics based retrieval scheme such as FSI insures that the
455 multipath can be correctly resolved.

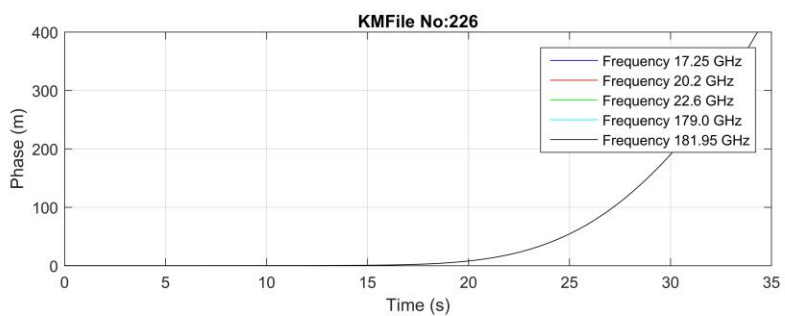
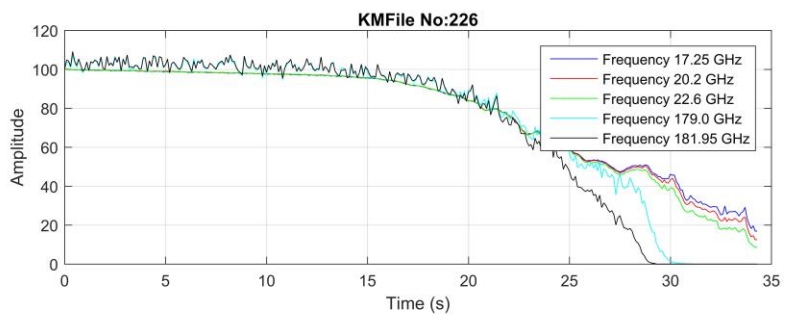
456

457 **4.2 Comparing KM based retrievals in turbulent and cloudy air with corresponding** 458 **values in the model**

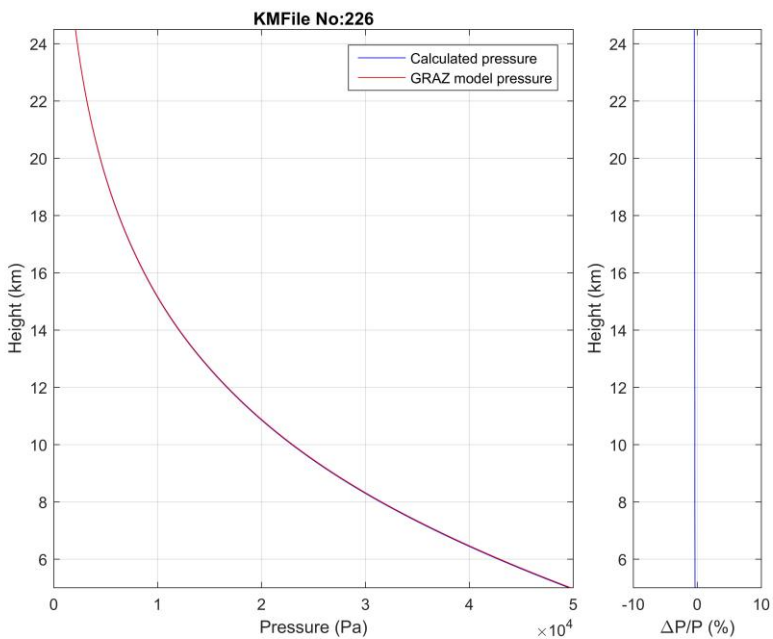
459 The forward simulation of the Leo-Leo radio occultation signals has here been performed
460 in turbulent and cloudy air for probing electromagnetic frequencies in the KM range.
461 Figure 6 (A) shows the amplitudes and phases for the 5 frequencies. It is seen especially
462 on the amplitudes that the signals are noisy due to scintillations caused by the cloudy
463 atmosphere. The result of the solver is presented in Figure 6 (B)-(D). These figures show
464 the calculated (blue curve) pressure, temperature and specific humidity profiles together
465 with the corresponding GRAZ (red curve) model profiles. The relative difference
466 between the retrieved physical parameters and the model values are represented with the
467 blue curves on the right side of the plots. It's seen from the plots that there is a relative
468 good agreement between retrieved atmospheric parameters and the model parameters
469 even for simulations in cloudy air.

470

471

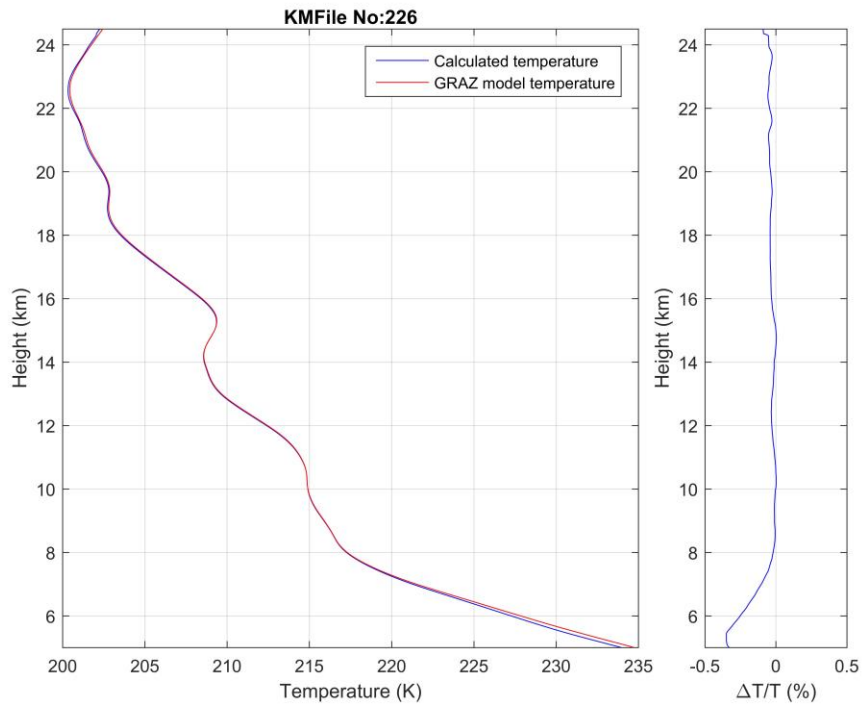


472 (A)

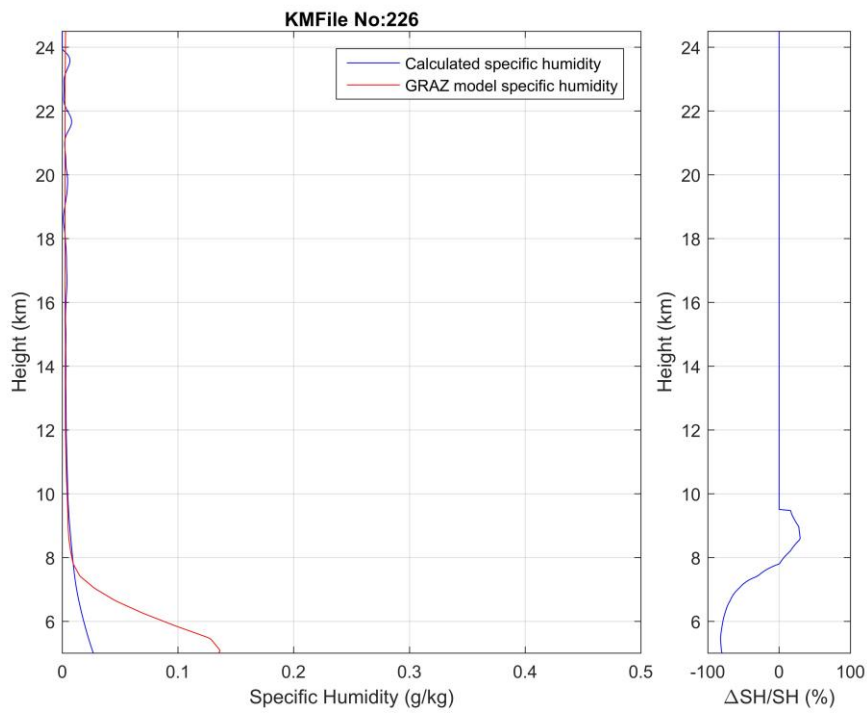


473

474 (B)



475 (C)



476

477 (D)

478 **Figure 6.** (A) The amplitude and phases for the 5 different KM frequencies. The mean
479 latitude and longitude for the tangent point is -55.42 degrees -30.86 degrees for this
480 setting occultation. (B) The pressure versus height. The blue curve is the retrieval while
481 the red curve is the GRAZ model. (C) The temperature versus height. The blue curve is
482 the retrieval while the red curve is the GRAZ model. (D) The specific humidity versus
483 height. The blue curve is the retrieval while the red curve is the GRAZ model. Panels (B)
484 to (D) all have a blue curve on the right side which is the relative difference between the
485 retrieved values and the GRAZ model values.

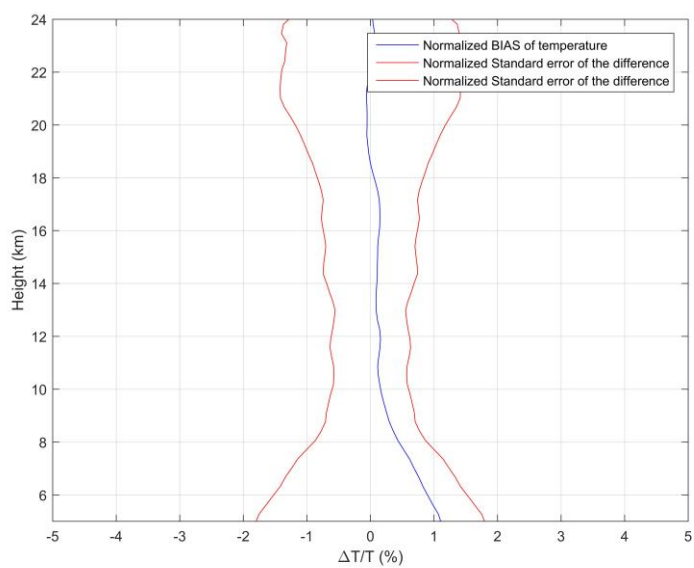
486

487 The specific humidity is again determined as expected with the lowest precision, but it is
488 still relative precise as long as all of the frequencies are present. The height at which the
489 radio wave is absorbed in the atmosphere increase with increasing probing frequency
490 leading to lower precision in the retrieved parameters.

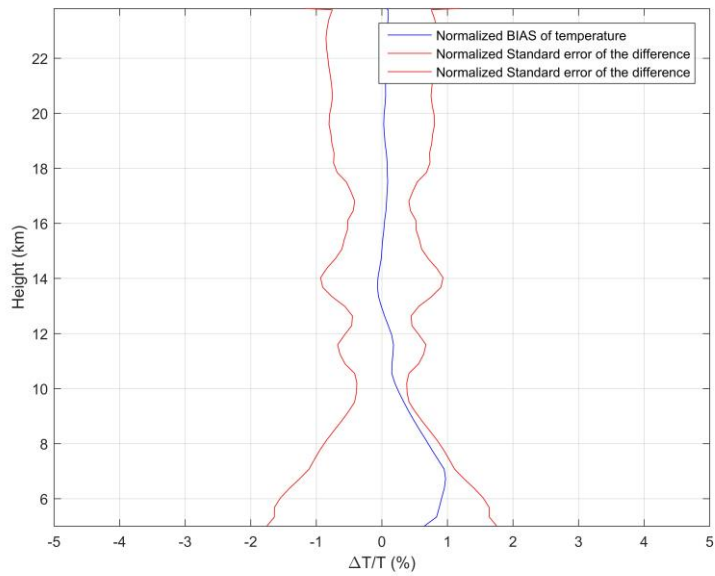
491 **4.3 Simulation class statistics**

492 Simulations have been performed for 4 different classes corresponding to different
493 frequency systems and noise levels. Figure 7 shows the statistics for the retrieved
494 temperature for simulation class 2, 3 and 4. It seen that the noise increases the error levels
495 compared to the corresponding clear air case. The increase in the error levels are however
496 modest due to appropriate low pass filtering of the radio occultation amplitudes and
497 phases.

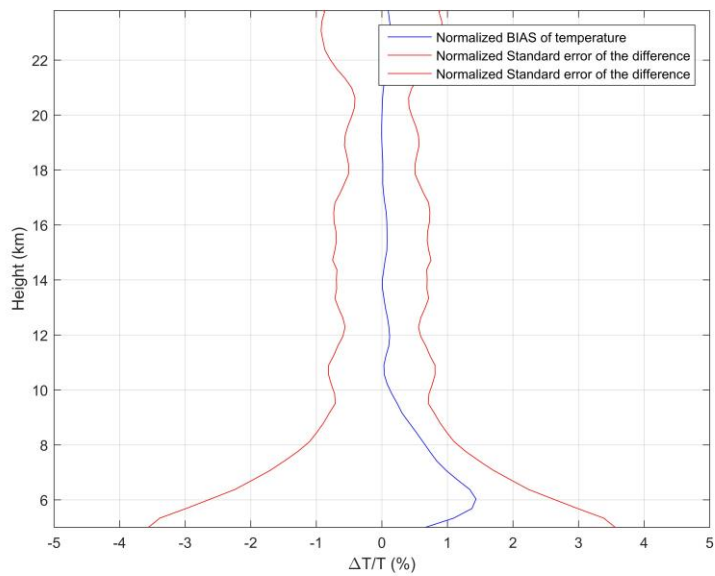
498



499 (A)



500 (B)



501 (C)

502 **Figure 7.** Panels (A) to (C). The normalized temperature bias (blue curve) and
 503 normalized standard error of the difference for temperature (red curve) in (%) as a
 504 function of height. (A) This is for Simulation Class 2. (B) This is for Simulation Class 3.
 505 (C) This is for Simulation Class 4.

506

507 In the current version of the retrieval chain extrapolated values are used when there are
508 no imaginary refractivity values. The imaginary refractivity corresponding to the high
509 frequencies in the KM range stops at a higher altitude than the values in the XK range.
510 This is the reason for the higher error level seen for probing frequencies in the KM range.
511 This issue can be solved using an extension of the imaginary refractivity (for these high
512 frequency probing radio waves) to lower altitudes. This extension can be based on
513 models in the same way bending angles are extended (due to a high noise level) at high
514 altitudes using statistical optimization in GPS-LEO radio occultations. Work on this
515 approach has been initiated.

516

517 It is seen that the bias and standard error of the difference all fall within an acceptable
518 error level. The presented simulations and retrievals of LEO-LEO cross links radio
519 occultations using high frequency probing radio waves have shown that this technique
520 can be used even in challenging conditions to retrieval valuable information on important
521 atmospheric parameters such as the atmospheric content of water vapor. Information that
522 can not directly be extracted from standard GPS-LEO radio occultations. The presented
523 retrieval chain is not a final operational chain and a number of things can be improved so
524 errors presented here is higher than what can be accomplished. The technique discussed
525 can also be used to retrieve other parameters such as the content of ozone. This is
526 accomplished by adding additional probing frequencies.

527 **5. Conclusion**

528 We have in this study presented a wave optics based LEO-LEO retrieval chain. The new
529 LEO-LEO radio occultation processing chain has been used on radio occultation
530 simulations provided by the University of Graz. These radio occultations use 5 different
531 XK or KM probing frequencies. Both radio occultations in clear air and in a turbulent
532 cloudy atmosphere for frequencies in the XK and KM frequency range have been studied.
533 The retrieval results were compared to the atmospheric parameters that are used to
534 generate the inputs to the wave optics propagator. The error levels are as expected higher
535 in the turbulent cloudy atmosphere compared to the error level in the clear air atmosphere.
536 Based on these comparisons it can be concluded that the wave optics based retrieval
537 chain gives good results for both XK and KM frequencies and the feasibility of the
538 measurement concept has been shown. The results are in general a little better in the XK
539 frequency range compared to the KM frequency. The reason for this is that the probing
540 KM frequency waves stop at higher heights than the XK frequency waves. This cause a
541 decrease in the precision of the solver results at low heights in the KM frequency based
542 system of equations. The plots presenting the bias and standard deviation of the
543 difference errors show an increase in the error level when the heights are decreasing. The
544 reason for this is that there is no measurements at low altitudes and the complex
545 refractivity values are therefore found from an extrapolation of the curves. This will in
546 many cases lead to an error in the retrieved parameters at low altitudes and hence an
547 increase in the error level. A method to overcome this has been mentioned in the paper.
548 The results of the simulations in this study show that it is possible to retrieve atmospheric

549 parameters such as water vapor with out external information using a microwave LEO-
550 LEO radio occultations technique. Future satellite missions could use this technique to
551 measure these parameters which in general are considered to be a challenge to measure.

552

553

554 **Acknowledgments**

555 This work was supported by ESTEC Contract No. 16743/02/NL/FF. The authors wish to
556 thank University of Graz for providing the simulated LEO-LEO radio occultations in the
557 XK and KM frequency range. Data used in this paper can be obtained from the authors.

558

559

560

561 **6. References**

562 Benzon, H.-H., and P. Hoeg (2015), Wave propagation simulation of radio occultations
563 based on ECMWF refractivity profiles, *Radio Sci.*, 50, doi: 10.1002/2015RS005649.

564

565 Born, M., and E. Wolf, *Principles of Optics*, Cambridge Univ. Press, New York, 1999.

566

567 Eriksson, P., Jimenez, C., Murtagh, D., Elgered, G., Kuhn, T., Buhler, Measurement of
568 tropospheric/stratospheric transmission at 10-35 GHz for H₂O retrieval in low Earth
569 orbiting satellite links. *Radio Sci.* Vol. 38, No. 4, 8069 doi:10.1029/2002RS002638 13
570 June 2003.

571

572 Fjeldbo, G., A. J. Kliore, and R. Eshlermann, The neutral atmosphere of Venus studied
573 with the Mariner V radio occultation experiments, *Astron. J.*, 76(2), 123-140, 1971.

574

575 Fritzer, J., G. Kirchengast, M. Pock, and V. Proschek (2010), End - to - End Generic
576 Occultation Performance Simulation and Processing System version 5.5 (EGOPS 5.5)
577 Software User Manual, Tech. Rep. ESA/ESTEC 1/2010, 490 pp., Wegener Cent. and
578 IGAM/Inst. of Phys., Univ. of Graz, Graz, Austria.

579

580 Gorbunov, M.E., Canonical transform method for processing GPS radio occultation data
581 in lower troposphere, *Radio Science*, 37(5), 10. 1029/2000RS002592, 9-1-9-10, 2002.

582

583 Gorbunov, M.E. and K. B. Lauritsen, Analysis of wave fields by Fourier Integral
584 Operators and its application for radio occultations, Radio Science, 2004, 39(4), RS4010,
585 doi:10.1029/2003RS002971, 2004.

586

587 Gorbunov, M. E., and G. Kirchengast, Fluctuations of radio occultation signals in X/K
588 band in the presence of anisotropic turbulence and differential transmission retrieval
589 performance, Radio Sci., 42, RS4025, doi:10.1029/2006RS003544, 2007.

590

591 Gorbunov, M. E., G. Kirchengast, Processing X//K band radio occultation data in the
592 presence of turbulence, RADIO SCIENCE, VOL. 40, RS6001,
593 doi:10.1029/2005RS003263, 2005.

594

595 Gorbunov, M. E., G. Kirchengast, Fluctuations of radio occultation signals in X/K band
596 in the presence of anisotropic turbulence and differential transmission retrieval
597 performance, RADIO SCIENCE, VOL. 42, RS4025, doi:10.1029/2006RS003544, 2007.

598

599 Høeg, P., and G. Kirchengast, ACE+ Atmosphere and Climate Explorer based on GPS,
600 GALILEO, and LEO-LEO Radio Occultation, Proposal to ESA in Response to the
601 Second Call for Proposals for Earth Explorer Opportunity Missions, 2002.

602

603 Jensen, A. S., M. S. Lohmann, H-H Benzon and A. S. Nielsen, "Full Spectrum Inversion
604 of radio occultation signals," Radio Sci., 38(3), 1040, doi:10.1029/2002RS002763, 2003.

605

606 Jensen, A. S., M. S. Lohmann, A. S. Nielsen, and H.-H. Benzon, Geometrical optics
607 phase matching of radio occultation signals, *Radio Sci.*, 39, RS3009, doi:
608 10.1029/2003RS002899, 2004.

609

610 Kirchengast, G., S. Schweitzer, J. Ramsauer, and J. Fritzer (2007), End-to-End Generic
611 Occultation Performance Simulator version 5.2 (EGOPsv5.2) Software User Manual
612 (Overview, Reference, and FileFormat Manual), Tech. Rep. ESA/ESTEC 4/2007,
613 Wegener Cent. And IGAM/Inst. of Phys., Univ. of Graz, Graz, Austria.

614

615 Kursinski, E. R, Leroy, S.S., and Herman, B, The Radio Occultation Technique, *Terr.*
616 *Atmos. Oceanic Sci.* 11, 53-114, 2000.

617

618 Kursinski, E. R., et al., A Microwave Occultation Observing System Optimized to
619 Characterize Atmospheric Water, Temperature, and Geopotential via Absorption, *Journal*
620 *of Atmospheric and Oceanic Technology*, 19, pp 1897-1914, 2002.

621

622 Liebe, H. J., MPM - an Atmospheric Millimeter-wave Propagation Model, *International*
623 *Journal of Infrared and Millimeter Waves*, vol. 10, No. 6, 1989.

624

625 Lohmann, M. S., A. S. Jensen, H-H Benzon, , and A. S. Nielsen, Application of window
626 functions for full spectrum inversion of cross-link radio occultation data, *Radio Science*
627 2006, doi 10.1029/2005RS003273.

628

629 Nielsen, A. S., M. S. Lohmann, P. Høeg, H.-H. Benzon, A. S. Jensen, T. Kuhn., C.
630 Melsheimer, S. A. Buehler, P. Eriksson, L. Gradinarsky, C. Jimenez, G. Elgered,
631 Characterization of ACE+ LEO-LEO Radio Occultation Measurements, ESTEC Contract
632 NO. 16743/02/NL/FF. 2003. This report can be obtained from the authors.

633

634 Hoeg, P., G. Kirchengast, ACE+: Atmosphere and Climate Explorer, Proposal to ESA,
635 see <http://www.dmi.dk/fileadmin/Rapporter/SR/sr02-07.pdf>, 2002.

636

637 Schweitzer, S., G. Kirchengast, M. Schwaerz, J. Fritzer, and M. E. Gorbunov,
638 Thermodynamic state retrieval from microwave occultation data and performance
639 analysis based on end-to-end simulations, *J. Geophys. Res.*, 116, D10301,
640 doi:10.1029/2010JD014850, 2011.

641

642 Sorensen, D. C., Newton's Method with a Model Trust Region Modification, *SIAM J.*
643 *Numer. Anal.*, 19(2), 409–426, 1982.

644